mater.scichina.com link.springer.com

Published online 7 December 2022 | https://doi.org/10.1007/s40843-022-2268-9
Sci China Mater 2023, 66(3): 944–954

Engineering chemical-bonded Ti_3C_2 MXene@carbon composite films with 3D transportation channels for promoting lithium-ion storage in hybrid capacitors

Min Feng[1], Wanli Wang[1], Zhaowei Hu[1], Cheng Fan[1], Xiaoran Zhao[1], Peng Wang[1], Huifang Li[1], Lei Yang[2,3], Xiaojun Wang[1,3*] and Zhiming Liu[1*]

ABSTRACT **Lithium-ion capacitors (LICs) are promising energy storage devices because they feature the high energy density of lithium-ion batteries and the high power density of supercapacitors. However, the mismatch of electrochemical reaction kinetics between the anode and cathode in LICs makes exploring anode materials with fast ion diffusion and electron transfer channels an urgent task. Herein, the two-dimensional (2D) Ti_3C_2 MXene with controllable terminal groups was introduced into 1D carbon nanofibers to form a 3D conductive network by the electrospinning strategy. In such Ti_3C_2 MXene and carbon matrix composites (named KTi-400@CNFs), the 2D nanosheet structure endows Ti_3C_2 MXene with more active sites for Li^+ ion storage, and the carbon framework is favorable to the conductivity of the composites. Impressively, Ti–O–C bonds are formed at the interface between Ti_3C_2 MXene and the carbon framework. Such chemical bonding in the composites builds a bridge for rapid electron transportation and quick ion diffusion in the longitudinal direction from layer to layer. As a result, the optimized KTi-400@CNFs composites maintain a good capacity of 235 mA h g^{-1} for 500 cycles at a current density of 5 A g^{-1}. The LIC consisting of the KTi-400@CNFs//AC configuration achieves high energy density (114.3 W h kg^{-1}) and high power density (12.8 kW kg^{-1}). This paper provides guidance for designing 2D materials and the KTi-400@CNFs composites with such a unique structure and superior electrochemical performance have great potential in the next-generation energy storage fields.**

Keywords: Ti_3C_2, carbon nanofibers, Ti–O–C chemical bonds, 3D transportation channels, lithium-ion capacitors

INTRODUCTION

With the continuous development of the world economy and the massive global spread of coronavirus, miniaturized electronic devices have become increasingly important in the fields of healthcare, carbon neutrality, and environmental protection energy. Hence, exploring new energy storage devices to power these smart devices is greatly desirable [1–4]. As a new energy storage device, lithium-ion capacitors (LICs) [5–8] are considered one of the most promising energy storage devices for portable electronics in the future, because they feature both a high energy density of lithium-ion batteries (LIBs) [9–11], and a high power density of supercapacitors (SCs) [12–15]. However, the cathode of LICs is a capacitive-type material that stores charge *via* adsorption/desorption, whereas the anode is a battery-type material that stores charge *via* Li^+ ion insertion/extraction [16]. The unbalanced charge storage kinetics make the development of LICs with ideal energy and power density still a challenge [17,18]. Thus, the exploration of high-rate anode materials to narrow the kinetics gap has become the key to realizing the LICs with high performance [19,20].

MXenes, as new two-dimensional (2D) materials, have received great attention due to their high conductivity, flexible interlayer space, and tailored surface chemistry [21,22]. Till now, almost 100 MXene variants have been theoretically proposed, such as $Ti_3C_2T_x$, Nb_2CT_x, and V_2CT_x [23–26]. Among them, $Ti_3C_2T_x$ MXene is the most widely studied owing to its potential large-scale application in LIBs and LICs with excellent pseudocapacitance performance [27–32]. Chen's group [33] prepared a fibrous hydroxylated Ti_3C_2/CNTs (h-Ti_3C_2/CNTs) composite, which displays abundant sodiophilic sites, satisfying thermal conductivity, and fast ion/electron transport kinetics. The terminal groups of $Ti_3C_2T_x$ MXene etched by LiF and hydrochloric acid generally contain –F groups, which are not favorable for the transportation of the electrolyte ions. Surface modification would be a hopeful strategy to control the type and content of terminal functional groups by replacing or eliminating highly electronegative ions [34–37]. Fan's group [38] reported an *n*-butyllithium-treated method to turn the –F and –OH terminal groups to –O groups on $Ti_3C_2T_x$ MXenes, and the *n*-butyllithium-treated $Ti_3C_2T_x$ MXene shows promising performance in pseudocapacitors. Although the electrochemical performance of the surface-modified MXene has been enhanced in LICs, the intrinsic flaws of 2D materials, such as interlayer agglomeration and blocked longitudinal ion transportation from layer to layer, are still main issues that need to be solved.

Scaffolding 3D channels between MXene layers for ion transportation is an essential route to address the inherent

[1] College of Electromechanical Engineering, Shandong Engineering Laboratory for Preparation and Application of High-performance Carbon-Materials, Qingdao University of Science & Technology, Qingdao 266061, China
[2] Research Center for Intelligent and Wearable Technology, College of Textiles and Clothing, Qingdao University, Qingdao 266071, China
[3] Key Laboratory of Advanced Energy Materials Chemistry (Ministry of Education), College of Chemistry, Nankai University, Tianjin 300071, China
* Corresponding authors (emails: wangxiaojunchem@163.com (Wang X); zmliu@qust.edu.cn (Liu Z))

defects of 2D materials [39–42]. Inspired by this, the surface modified $Ti_3C_2T_x$ MXene was rationally embedded into 1D carbon nanofibers (CNFs) using the electrospinning method (named KTi-400@CNFs). In the composites of KTi-400@CNFs, the 1D carbon matrix shortens the ion diffusion path to improve carrier transport dynamics, and the 2D $Ti_3C_2T_x$ MXene nanosheets offer more active sites to contribute high specific capacitance [43,44]. Significantly, the chemical bond of Ti–O–C is formed at the interface of the 1D CNFs and 2D MXene nanosheets, which not only inhibits the agglomeration of MXene but also sets up 3D channels for ion transportation between MXene layers. Owing to the flexibility of intra-layer planar transportation and inter-layer longitudinal transportation of ions and electrons, the electrochemical reaction kinetics of the composites would be significantly enhanced. Correspondingly, when used as the anode of LICs, KTi-400@CNFs exhibit an excellent energy density (114.3 W h kg^{-1}) and outstanding power density (12.8 kW kg^{-1}). Impressively, the reaction mechanism of KTi-400@CNFs//AC LICs also demonstrates the smooth insertion/extraction of Li^+ ions from the KTi-400@CNFs composites. Such structural construction and superior electrochemical performance of KTi-400@CNFs will provide a new reference for the design of 2D materials in advanced energy storage techniques [45–49].

EXPERIMENTAL SECTION

Synthesis of $Ti_3C_2T_x$ MXene

First, 1 g of LiF and 20 mL of hydrochloric acid solution (12 mol L^{-1}) were added to the PTFE liner and stirred at room temperature. Afterward, 1 g of Ti_3AlC_2 powder was slowly added to it and etched at 35°C for 24 h. Then, the obtained solution was washed with deionized water (DIW) to remove residual hydrofluoric (HF) acid and impurities until the pH value was 6–7. Finally, the resulting precipitate was freeze-dried for more than 12 h to obtain the $Ti_3C_2T_x$ MXene.

Ion intercalation and surface modification of $Ti_3C_2T_x$ MXene

$Ti_3C_2T_x$ MXene was dispersed in 1.8 mol L^{-1} KOH solution and stirred under an Ar atmosphere for 4 h. Subsequently, it was washed several times with DIW, and the obtained precipitate was freeze-dried. The obtained product was named KOH-Ti_3C_2. Finally, KOH-Ti_3C_2 was calcined in an Ar atmosphere at 673 K, and the obtained powder was named KOH-Ti_3C_2-400 (KTi-400).

Synthesis of KTi-400@CNFs

First, 1 g of polyacrylonitrile (PAN) powder was added to 7 mL of *N*,*N*-dimethylformamide (DMF) and stirred until it became homogeneous. Afterward, different proportions of KTi-400 were added and stirred at room temperature to obtain a homogeneous spinning solution precursor. The precursor was loaded into a 10-mL plastic syringe fitted with an 18 G needle. A voltage of 18 kV was applied to the needle tip during rotation while grounding the collector covered with aluminum foil. The distance between the needle tip and collector was approximately 18 cm, and the pushing rate was controlled at 0.6 mL h^{-1}. The samples were electrostatically spun at a relative humidity of less than 50%. The films obtained by electrospinning were first stabilized in air at a heating rate of 5°C min^{-1} to 250°C for 1 h and then carbonized in an Ar atmosphere at a heating rate of 5°C min^{-1} to 600°C for 4 h to obtain the flexible KTi-400@CNFs electrode. For comparison, the Ti_3C_2@CNFs electrode was also prepared using electrospinning-untreated Ti_3C_2 MXene with PAN.

Material characterization

The phase purity and crystal structure of the substances were identified *via* X-ray diffraction (XRD, MiniFlex 600) using Cu-Kα radiation (λ = 0.154187 nm) with radiation conducted at 2θ angles of 3°–90°. The morphology and microstructure were observed using scanning electron microscopy (SEM, Hitachi SU8010) and transmission electron microscopy (TEM, FEI Tecnai F20). Surface chemistry and binding energy were analyzed by X-ray photoelectron spectroscopy (XPS, K-Alpha). Fourier transform infrared (FTIR) spectra were collected through Nicolet IS50. The weight content of MXene was determined through thermogravimetric analysis (TGA, TG-209F3) from room temperature up to 900°C at a heating rate of 10°C min^{-1} under flowing air.

Fabrication of the half-cells and LICs

The flexible KTi-400@CNFs electrode was directly punched for the use as the working electrode without any other treatments. In the half-cells, the lithium metal was used as the anode, Celgard 2400 as the separator, and 1.15 mol L^{-1} $LiPF_6$ in ethylene carbonate/ethyl methyl carbonate/dimethyl carbonate (1:2:2, *v*/*v*/*v*) as the electrolyte. The whole assembly process of the coin cell was performed in an Ar-filled glove box. Before assembling the LICs, the KTi-400@CNFs were pre-lithiated in Li-ion half-cells. The half-cells were cycled five times in the voltage range of 0.01–3.0 V at a current density of 0.1 A g^{-1}, followed by discharging to 0.01 V at a current density of 0.05 A g^{-1}. Subsequently, the pre-lithiated KTi-400@CNFs were used as the anode, and the AC obtained *via* vacuum extraction (where YP50F:single walled carbon nanotubes = 7:3) was used as the cathode to fabricate the LICs. And the mass ratio of the anode and cathode materials is approximately 1:3–1:5. The half-cells were tested at room temperature in the voltage range of 0.01–3.0 V, and the LICs were tested in the voltage range of 1.0–3.8 V.

Electrochemical measurements

Electrochemical measurements were performed using CR2032 coin-type cells. The half-cells and LICs were assembled in a glove box. The half-cell charge and discharge performance were tested using the LAND battery test system (Wuhan LAND Electronics Co., Ltd., China). The cyclic voltammetry (CV) curves and galvanostatic charge-discharge (GCD) curves of the LICs were obtained by a CHI-760E electrochemical workstation (Chenhua, Shanghai, China). Electrochemical impedance spectroscopy (EIS; test frequency from 10^5 to 0.01 Hz) curves were obtained *via* the Ivium test system. The galvanostatic intermittent titration (GITT) was used to calculate the Li^+ diffusivity coefficient. The Li^+ diffusivity coefficient was calculated based on the following equation:

$$D = \frac{4L^2}{\pi\tau}\left(\frac{\Delta E_t}{\Delta E_s}\right)^2, \quad (1)$$

where τ is the relaxation time (s), L is the diffusion length (cm) of Li^+, which is equal to the thickness of the electrode, ΔE_s is the steady-state potential change (V) by the current pulse, ΔE_t is the potential change (V) during the constant current pulse after eliminating the *iR* drop. A current pulse of 50 mA g^{-1} was

applied for 10 min, and the following relaxation time was 15 min.

In addition, the specific capacitance (C, F g^{-1}), energy density (E, W h kg^{-1}), and power density (P, W kg^{-1}) of the LICs were calculated using the following equations:

$$C = \frac{I\,\Delta t}{m\,\Delta V}, \tag{2}$$

$$E = \frac{1}{2}C\,(\Delta V)^2, \tag{3}$$

$$P = \frac{E}{t}, \tag{4}$$

where I is the discharge current (A), Δt is the discharge time (s), m is the sum of the active mass of the anode and cathode (g), ΔV is the voltage interval (V), and t is the discharge time (h).

RESULTS AND DISCUSSION

The composites of the surface-modified Ti_3C_2 MXene and 1D CNFs, KTi-400@CNFs, were synthesized by a simple electrospinning process, as shown in Fig. 1. First, Ti_3AlC_2 was etched with HF acid generated *in situ* from LiF and hydrochloric acid to obtain Ti_3C_2 MXene, which contains several functional groups, such as –F and –OH, on its surface. Afterward, KTi-400 was obtained through K^+ ion intercalation and surface modification, which can increase the layer spacing and replace some –F and –OH with –O functional groups. Finally, KTi-400 nanosheets were embedded into CNFs using the electrospinning strategy. After high-temperature calcination, KTi-400 and CNFs were linked by the Ti–O–C bond. The presence of the Ti–O–C bond not only suppresses the interlayer agglomeration but also sets up the 3D transportation channels for ions and electrons between Ti_3C_2 MXene layers. Furthermore, the KTi-400@CNFs composites displayed excellent flexibility, and could be cut into desired sizes and directly serve as the anode of advanced LICs, where neither nonconductive binders nor current collectors were needed. In addition, we compared the effects of different contents of KTi-400 on the properties of the composites, i.e., 7-, 10-, and 16-KTi-400@CNFs (the content of KTi-400 was 7, 10, and 16 wt.%), respectively.

As shown in Fig. 2a, b, the Ti_3C_2 MXene, after the etching treatment, shows a distinct accordion-like structure compared with Ti_3AlC_2 (Fig. S1), indicating a successful exfoliation. Moreover, a lattice spacing of approximately 1.214 nm, corresponding to the (002) crystal plane of Ti_3C_2, can be observed in the high-resolution TEM (HRTEM) image of Ti_3C_2 (Fig. 2c). The layer spacing of Ti_3C_2 after the KOH treatment increases to 1.363 nm (Fig. 2d), which indicates that the K^+ ions are successfully embedded into the Ti_3C_2 MXene layers. The increased

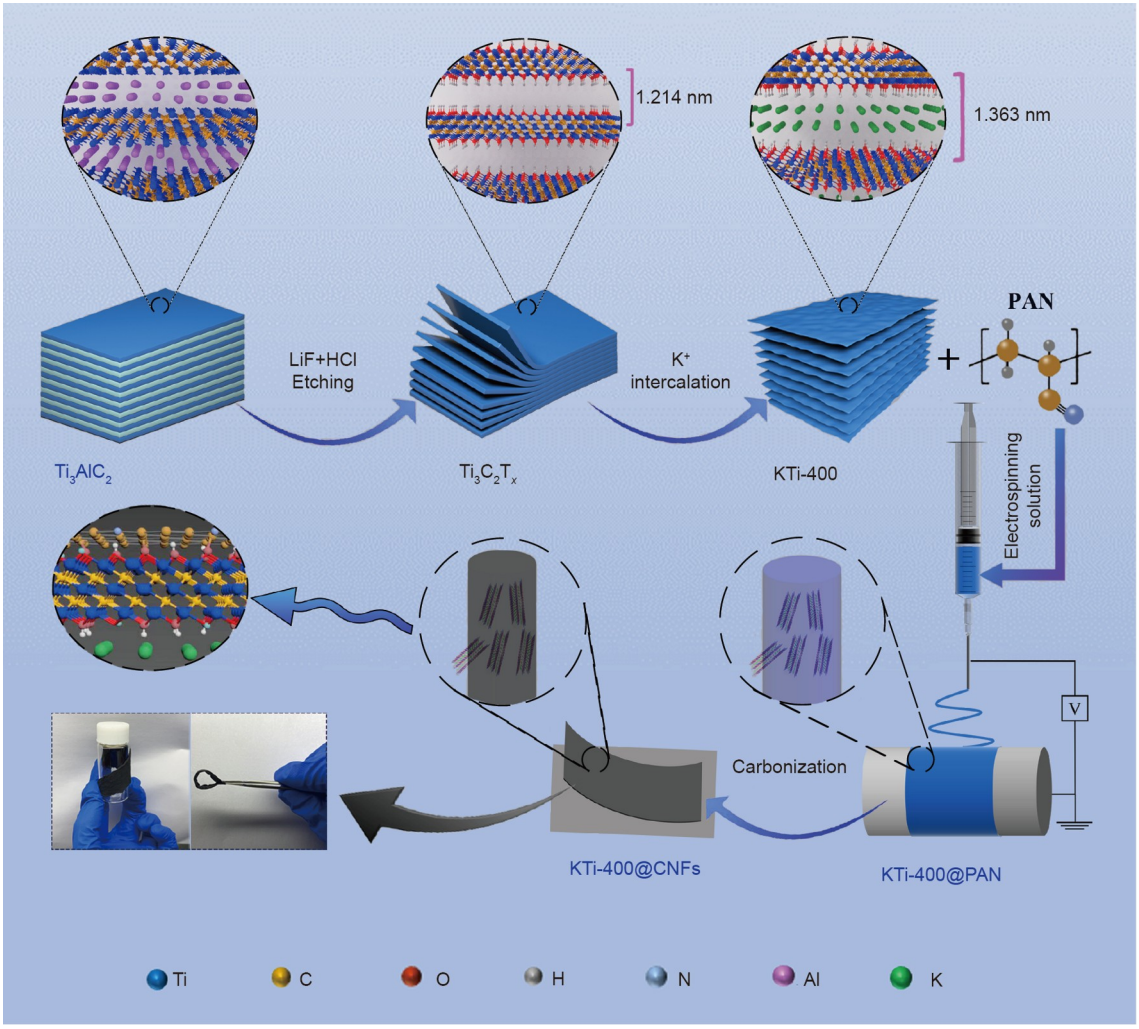

Figure 1 Schematic illustration of the preparation of the self-supported KTi-400@CNFs films.

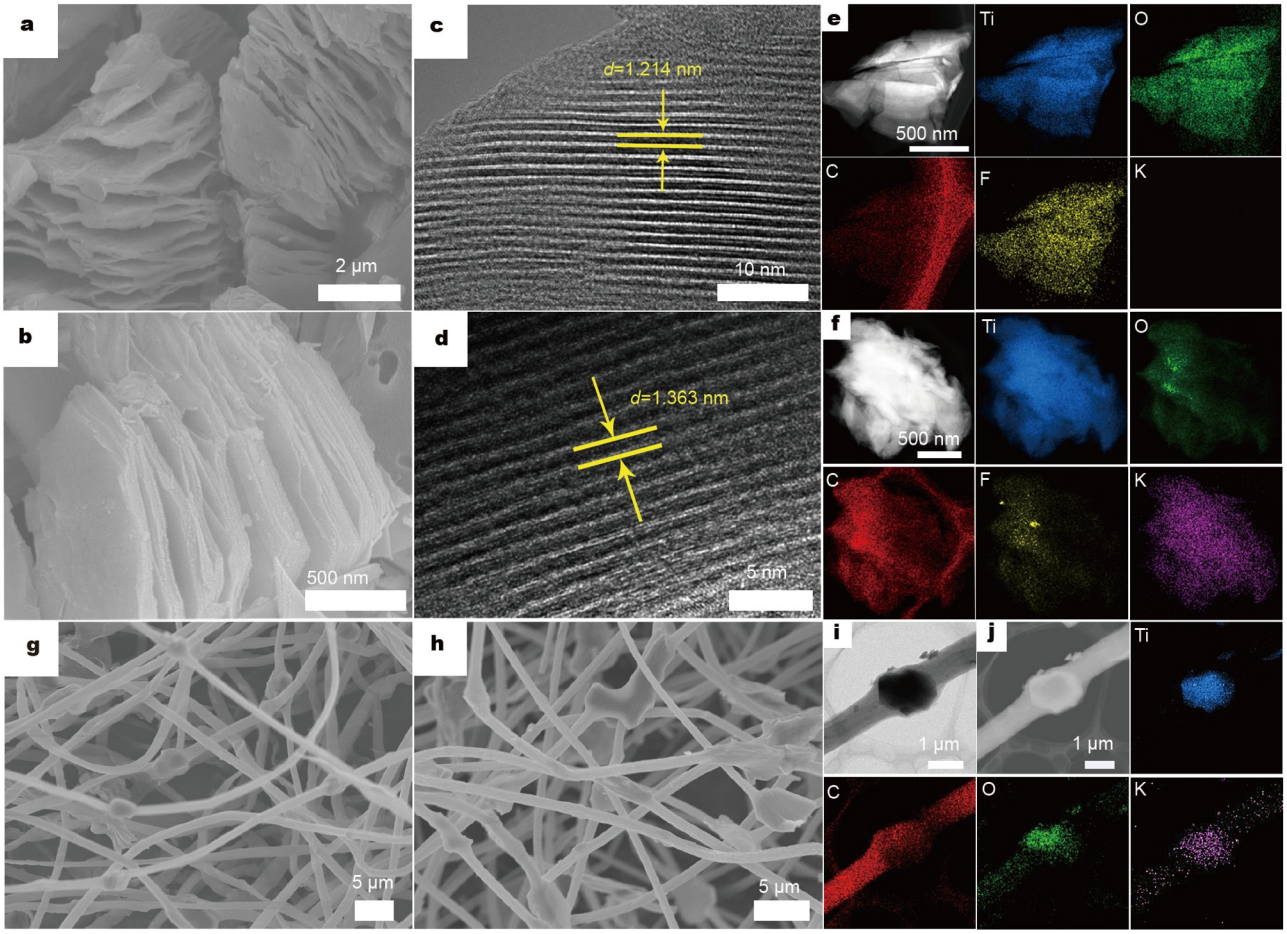

Figure 2 (a, b) SEM images of $Ti_3C_2T_x$ and KTi-400; (c, d) HRTEM images of $Ti_3C_2T_x$ and KTi-400; (e, f) scanning TEM (STEM) images with the corresponding elemental mapping of $Ti_3C_2T_x$ and KTi-400; (g, h) SEM images of 10-KTi-400@CNFs before and after carbonization; (i) TEM image of 10-KTi-400@CNFs; (j) STEM images with the corresponding elemental mapping of 10-KTi-400@CNFs.

layer spacing can provide more Li^+ ion storage active sites and shorten the ion diffusion path, which is beneficial for electrochemical performance. The elemental distribution in the composites was analyzed using energy-dispersive spectroscopy elemental mapping. Fig. 2e, f show that the Ti and C elements are uniformly distributed throughout the substrate. In addition, the F element was observed in the MXene nanosheets, which came from the HF acid generated during the etching process. Furthermore, a uniform distribution of the K element was observed in KTi-400 due to the introduction of K^+ ions, and the K element is absent in Ti_3C_2. Fig. 2g, h display the SEM images of 10 wt.% KTi-400@CNFs (10-KTi-400@CNFs) before and after calcination. The SEM images show that the CNFs form a 3D conductive network structure. After carbonization, the fibers can maintain their network morphology, which can provide high conductivity for the composites. The TEM images and elemental distribution of 10-KTi-400@CNFs (Fig. 2i, j) also show that MXene is embedded into the fibers and the Ti, C, O, and K elements are uniformly distributed in the composites, which forms 3D channels for ion transportation in the intra- and interlayers of 10-KTi-400@CNFs composites.

Fig. 3a, b show the XRD patterns of the Ti_3AlC_2, Ti_3C_2, KOH-Ti_3C_2, and KTi-400 samples. Comparing Ti_3AlC_2 with Ti_3C_2, after etching, the (104) peak in the outer plane of Ti_3AlC_2 was significantly weakened, whereas a (002) peak corresponding to the in-plane diffraction appeared in Ti_3C_2, indicating the successful fabrication of Ti_3C_2 MXene. When Ti_3C_2 MXene was treated with a KOH solution, the (002) peak shifted to a lower angle, which is due to the widening of the layer spacing caused by the successful embedding of K^+ ions into Ti_3C_2 MXene. These results also correspond to the SEM results in Fig. 2. Increased MXene layer spaces offer more active sites and smooth channels for Li^+ ion insertion/extraction and transportation in the plane. Fig. 3c shows the XPS spectra of Ti_3C_2 and KTi-400. As shown in the Ti_3C_2 spectrum, the Al layer is removed, and the surface is terminated by –F. After the KOH treatment, –OH will replace some –F. This is because the dissociation energy of the Ti–F bond is ~569 ± 33 kJ mol^{-1} and that of the Ti–O bond is ~666.5 ± 5.6 kJ mol^{-1}, and the substitution reaction of –F with –OH is inclined to occur in the alkaline solution. After calcination at 400°C, the F 1s peak and O 1s summit significantly decreased, while the K peak appeared. As a result, most of the –OH and –F groups would be removed, indicating the types of terminal groups of Ti_3C_2 MXene that can be controlled by the annealing process. In particular, the terminal groups of –F and –OH will hinder the diffusion of ions and thus reduce the capacitive performance of the electrode. Therefore, removing a part of the –F and –OH functional groups through high-temperature calcination is beneficial to the improvement of Li^+ ion storage capacitance. Fig. 3d displays that the peak intensity of the Ti–C

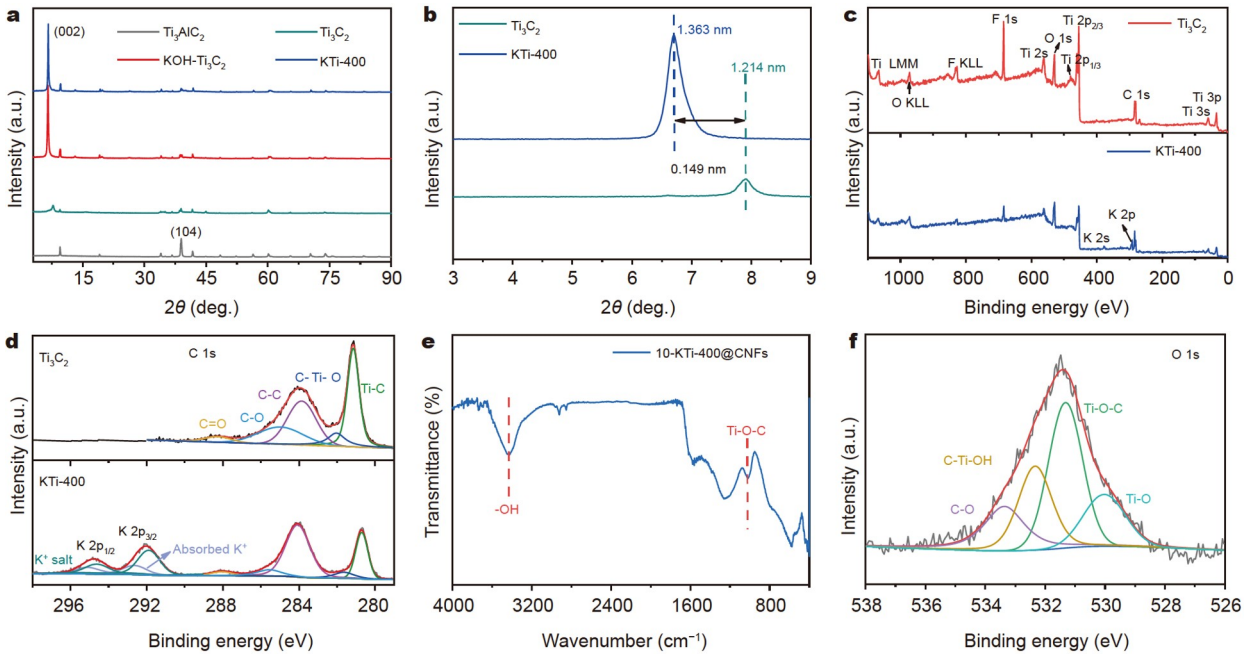

Figure 3 (a) XRD patterns of the Ti_3AlC_2, Ti_3C_2, KOH-Ti_3C_2, and KTi-400 samples, respectively; (b) magnification of XRD patterns in (a); (c) XPS spectra of Ti_3C_2 and KTi-400; (d) high-resolution XPS spectra of C 1s and K 2p of Ti_3C_2 and KTi-400; (e) FTIR spectra of 10-KTi-400@CNFs; (f) high-resolution XPS spectra of O 1s of 10-KTi-400@CNFs.

bond at approximately 281.2 eV in KTi-400 is lower than that in the Ti_3C_2 samples. The possible reason is that some of the amorphous carbon was formed during the acid etching process and removed after the calcination treatment [36]. In addition, the existence of the K $2p_{3/2}$ and K $2p_{1/2}$ orbitals at 292.0 and 294.8 eV confirm the successful embedding of K^+ ions in the KTi-400 sample. In the XPS spectrum in Fig. S2, the K 2p peak of KTi-400 is divided into two peaks, i.e., K^+ salt and adsorbed K^+ (Fig. S2a). The peaks of Ti 2p show that the intensity of the Ti–C and Ti–O peaks of KTi-400 is lower than that of Ti_3C_2 (Fig. S2b). Based on the XPS spectra of O 1s and F 1s (Fig. S2c, d), the C–Ti–OH, C–Ti–O, and Ti–O peaks were enhanced after the KOH treatment, whereas the intensity of Al–F and Ti–F was weakened, which is mainly caused by the partial replacement of –F by the –OH and –O groups.

The FTIR and XPS measurements were performed to investigate the interconnection between KTi-400 MXene and CNFs in 10-KTi-400@CNFs composites. The FTIR spectrum of Fig. 3e exhibits that the –OH and C=C bonds are represented at 3432.9 and 1586.7 cm^{-1}, respectively. Significantly, a new chemical bond of Ti–O–C appeared at 1027 cm^{-1}, which indicates the KTi-400 MXene is combined with CNFs through chemical bond. As a comparison, the FTIR spectrum of the pristine MXene is shown in Fig. S3, which excludes the peak of Ti–O–C bonds at 1027 cm^{-1}. The result implies that the chemical bond is most likely achieved by the –O terminal groups at the interface of KTi-400. Impressively, the O 1s spectrum of 10-KTi-400@CNFs was also analyzed and is depicted in Fig. 3f. In addition, the C–O, C–Ti–OH, and Ti–O bonds can be found at 533.4, 532.3, and 530.0 eV, respectively. A new peak at 531.3 eV corresponding to the Ti–O–C bond also appeared. Such results demonstrate the formation of the Ti–O–C bond at the interface between KTi-400 MXene and the carbon matrix, which provides smooth 3D transportation channels for ion diffusion and electron transportation. Fig. S4 illustrates the content of KTi-400 MXene in 7-, 10-, and 16-KTi-400@CNFs, which was estimated by TGA. There is a little weight loss until 300°C, which is mainly attributed to the removal of water and DMF between MXene layers. When the calcination temperature was increased to 900°C, the remaining powder was TiO_2. Based on the TGA results and calculation, the weight fraction of KTi-400 MXene in 10-KTi-400@CNFs was 41.2%.

The prepared 10-KTi-400@CNFs films were directly used as anodes for the coin-type half-cells to study their electrochemical properties. Fig. 4a displays the CV curves of the 10-KTi-400@CNFs composites at 0.1 mV s^{-1} with a potential ranging from 0.01 to 3.0 V (*vs.* Li/Li^+). During the first discharge, an irreversible reduction peak appeared at approximately 0.8 V, which may be a result of the electrolyte decomposition and the formation of the solid electrolyte interface (SEI) layer. In the subsequent cycles, the reduction peak at 0.8 V disappeared, indicating that a stable SEI film was formed in the first cycle. Starting from the second cycle, the intensity of the broad anode peak at 1.5 V and the cathode peak at 1.3 V overlapped well with no shifts in the position, implying good reversibility of Li^+ ion insertion/extraction in the 10-KTi-400@CNFs. Fig. 4b exhibits the GCD curves of 10-KTi-400@CNFs for the first three cycles at a current density of 0.1 A g^{-1}. In the first discharge curve, a plateau at approximately 0.8 V was observed, which is consistent with the CV results. However, in the subsequent GCD curves, no significant plateau was found because 10-KTi-400@CNFs provide fast diffusion kinetics for Li^+ ions. This is mainly due to the presence of Ti–O–C bonds that ensure fast ion transportation, not only in-plane but also between the layer-to-layer. At a current density of 0.1 A g^{-1}, the 10-KTi-400@CNFs had a discharge-specific capacity of 855.5 mA h g^{-1} and charge-specific capacity of 649.7 mA h g^{-1} in the first cycle with an initial Coulombic efficiency (CE) of 75.9%. The irreversible capacity is

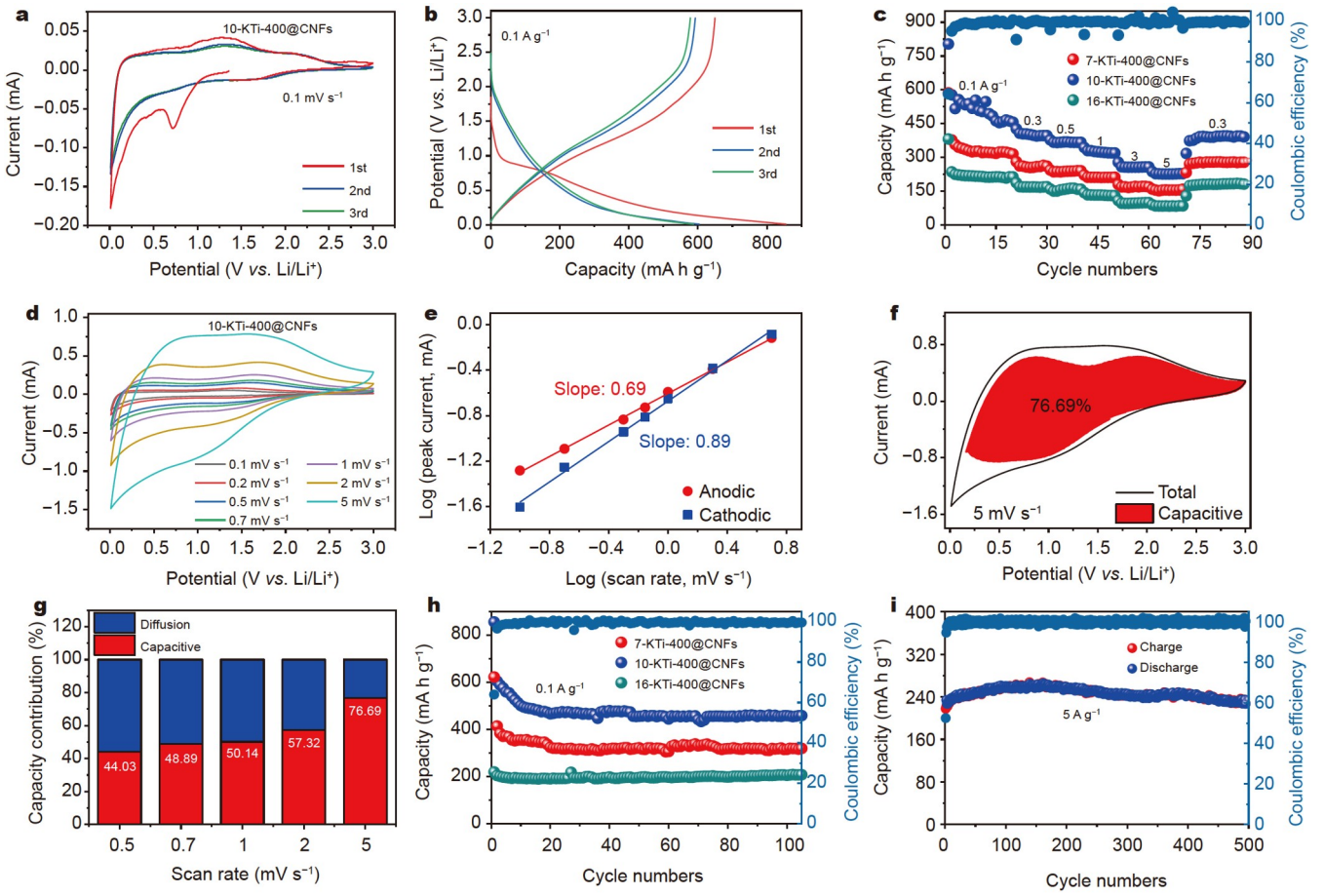

Figure 4 Electrochemical performance of the KTi-400@CNFs composites. (a) CV and (b) GCD curves of 10-KTi-400@CNFs; (c) rate performance of 7-, 10-, and 16-KTi-400@CNFs at different current densities; (d) CV curves of 10-KTi-400@CNFs at different scan rates; (e) Ragone plot of log (*i*, peak current) *vs.* log(*v*, scan rate) for 10-KTi-400@CNFs; (f) CV curves with the capacitive contribution of 10-KTi-400@CNFs at 5 mV s^{-1}; (g) capacitive contributions at various scan rates; (h) cycling performance of 7-, 10-, 16-KTi-400@CNFs at 0.1 A g^{-1}; (i) long cycling performance of 10-KTi-400@CNFs at a current density of 5 A g^{-1}.

mainly caused by the formation of an SEI film and the occurrence of some irreversible side reactions. In the second and third cycles, the CE reached more than 98%, and the reversible capacity was maintained at approximately 594.1 mA h g^{-1}. The high capacity as well as the high CE benefits from the K^+ ions intercalation stabilizing the interlayer structure of MXene and the 3D conductive network structure ensuring the intimate contact between CNFs and MXene.

To realize the optimal electrochemical performance in terms of capacity and rate capability, the mass ratio between KTi-400 and the carbon matrix should be optimized. Fig. 4c shows the rate performance of 7, 10, and 16 wt.% KTi-400@CNFs (7-, 10-, and 16-KTi-400@CNFs). The 10-KTi-400@CNFs had the highest specific capacities of 503.7, 401.6, 367.3, 330.3, 258.4, and 226.5 mA h g^{-1} at current densities of 0.1, 0.3, 0.5, 1, 3, and 5 A g^{-1}. Compared with 7- and 16-KTi-400@CNFs, the capacity of 10-KTi-400@CNFs at current densities of 0.1 A g^{-1} was greatly enhanced. When the KTi-400 content was 10 wt.%, the respective advantages of MXene and CNFs can be fully utilized, resulting in superior capacity and rate capability. The low loading of KTi-400 MXene in 7-KTi-400@CNFs (26.4%, Fig. S4) provided few active sites but high conductivity, so the 7-KTi-400@CNFs exhibited low capacity but a high rate capability. By contrast, the high loading of KTi-400 MXene in 16-KTi-400@CNFs (59.3%, Fig. S4) led to a low capacity and inferior rate capability, which is mostly due to the MXene not being embedded in CNFs, thus hindering the ion storage and diffusion in the longitudinal direction.

To further investigate the underlying reason for the superior rate performance of 10-KTi-400@CNFs, the kinetics behavior was also analyzed. Fig. 4d displays the CV curves at different scan rates (0.1, 0.2, 0.5, 0.7, 1, 2, and 5 mV s^{-1}). The potential of the redox peaks of the CV curves did not significantly change with the increase in the scan rate, implying the fast charge transfer process and enhanced electrochemical kinetics. In general, the ion storage mechanism of the electrode material can be plotted by the relationship between the peak current (*i*) and scan rate (*v*).

$$i = av^b, \tag{5}$$

$$\lg(i) = b\lg(v) + \lg(a), \tag{6}$$

where *i* and *v* denote the current density and scan rate, respectively, and *a* and *b* are the variable parameters. The value of *b* can be calculated from the slope of lg(*v*) and lg(*i*). A *b* value of 0.5 corresponds to the ideal type of a diffusion-controlled process, while a *b* value of 1 is for the ideal surface-controlled

process. As shown in Fig. 4e, the b values corresponding to the anode and cathode peaks are 0.69 and 0.89, respectively, indicating that the ion storage is dominated by the surface-controlled pseudocapacitive behavior. In addition, the contribution of the pseudocapacitive behavior and diffusion-controlled process at different scan rates can be calculated using the following equation:

$$i(V) = k_1 v + k_2 v^{1/2}, \quad (7)$$

where $k_1 v$ and $k_2 v^{1/2}$ denote the capacitive contribution and diffusion control contribution, respectively, and k_1 is a constant that can be calculated from the slope of i (response current) and V (given voltage). Fig. 4f, g present the capacity share of the diffusion-controlled and capacitance-controlled behaviors at different scan rates. The red area in Fig. 4f corresponds to the capacity of the capacitive control of 10-KTi-400@CNFs at 5 mV s^{-1}, and the calculated percentage is approximately 76.69%. Even at a scan rate of 0.5 mV s^{-1}, the contribution of the capacitive control can still reach 44.03% (Fig. 4g). The high capacitance contribution mainly comes from the abundant Li^+ ion storage sites on the MXene surface, which facilitates the charge transfer and storage.

Fig. 4h displays the cycling performance of 7-, 10-, and 16-KTi-400@CNFs at a current density of 0.1 A g^{-1}. The 10-KTi-400@CNFs discharged a specific capacity of 855.5 mA h g^{-1} in the first cycle with a very low CE of 75.9%. This result can be attributed to the irreversible decomposition of the electrolyte and the formation of the SEI film. After 140 cycles, a capacity of 458.8 mA h g^{-1} can be maintained. By contrast, the capacities of 7- and 16-KTi-400@CNFs were only 314.5 and 213.1 mA h g^{-1} at a current density of 0.1 A g^{-1}, respectively. The cycling performance of 7-, 10- and 16-KTi-400@CNFs at a current density of 0.5 A g^{-1} are given in Fig. S5, and the capacity comparison trend is the same as that at a current density of 0.1 A g^{-1}. This difference is mainly due to the optimal synergy between MXene and CNFs in the 10-KTi-400@CNFs composites. The increased active sites, shortened ion diffusion paths, and the opening of 3D transportation channels between the layers provide a guarantee of high capacity. The exceptional rate behavior and excellent cycle stability at the low current density of the 10-KTi-400@CNFs composites encourage us to further evaluate its long-term cyclic durability at a high current density. Impressively, the 10-KTi-400@CNFs still achieved a high specific capacity of 234.2 mA h g^{-1} and a high capacity retention of 98% after 500 cycles, even at 5 A g^{-1}. The superior cycling stability is ascribed to the synergistic effect of the K^+ ion and CNFs, which can stabilize not only the 2D layer structure but the 3D network framework of the 10-KTi-400@CNFs composites (Fig. 4i).

Furthermore, to illustrate the advantages of K^+ ion intercalation and surface modification of –O functional groups, the structure and electrochemical performance of 10 wt.% Ti_3C_2@CNFs (10-Ti_3C_2@CNFs) and 10-KTi-400@CNFs were compared. Fig. S6a shows the EIS plots of 10-Ti_3C_2@CNFs and 10-KTi-400@CNFs. The 10-KTi-400@CNFs displayed a small charge transfer impedance represented by the semicircle in the high-frequency region, indicating their fast charge transfer kinetics. This is mainly because the K^+ ion intercalation increases the MXene layer spacing, thus accelerating ion transportation and exchange. In addition, the substitution of –O terminal groups plays a positive role in the electrochemical performance. The cycling stability and rate performance of 10-Ti_3C_2@CNFs are shown in Fig. S6b, c. The specific capacity of 10-Ti_3C_2@CNFs is only 252 mA h g^{-1} at a current density of 0.1 A g^{-1} after 100 cycles, which is lower than that of 10-KTi-400@CNFs. Apart from the low capacity, the 10-Ti_3C_2@CNFs electrodes also exhibited an inferior rate capability. The capacities of 237.0, 173.3, 150.4, 115.6, 66.6, and 46.7 mA h g^{-1} can be obtained at current densities of 0.1, 0.3, 0.5, 0.7, 1, 3, and 5 A g^{-1}, respectively. When the current density returned to 0.3 A g^{-1}, the specific capacity just retained 190.5 mA h g^{-1}. The outstanding cycling stability and rate performance of the 10-KTi-400@CNFs prove that it is effective and feasible to increase the active sites and structural stability through K^+ ion intercalation and to improve the Li^+ ion storage capacity by modifying the functional groups. Fig. S6d, e display the CV curves of 10-Ti_3C_2@CNFs at 0.1 mV s^{-1} at different scan rates, respectively. During the first discharge cycle, a reduction peak appeared around 0.75 V, which is due to the formation of the SEI film and the occurrence of some irreversible reactions. The following CV curves overlapped well. However, the peak of around 0.75 V disappeared in the subsequent cycles. Based on the CV curves at different scan rates, the b values of the anode and cathode peaks were calculated as 0.67 and 0.86, respectively, which are slightly lower than those of 10-KTi-400@CNFs (Fig. S6f). The results show that the 10-KTi-400@CNFs have a higher pseudocapacitance contribution and are more favorable for fast Li^+ ion kinetics than 10-Ti_3C_2@CNFs. The high capacitance contribution also lays the foundation for its application in capacitors. The Li^+ diffusion behavior of the composites was further investigated using the GITT. Fig. S7 exhibits the GITT curves of 10-KTi-400@CNFs and 10-Ti_3C_2@CNFs, which were collected at 50 mA g^{-1} with discharging/charging for 10 min and rest for 15 min. The average Li^+ diffusion coefficients (D_{Li^+}) of 10-KTi-400@CNFs were 3.01×10^{-9} cm^2 s^{-1} during discharging and 2.81×10^{-9} cm^2 s^{-1} during charging, which is larger than those of 10-Ti_3C_2@CNFs (2.81×10^{-9} cm^2 s^{-1} during discharging and 2.58×10^{-9} cm^2 s^{-1} during charging). The advantage of Li^+ diffusion in 10-KTi-400@CNFs is attributed to the Ti–O–C bond, which ensures the fast diffusion of ions between layers.

The good cycling stability and excellent rate performance of the 10-KTi-400@CNFs electrode make it a promising anode for LICs. Therefore, 10-KTi-400@CNFs were used as the anode coupled with a commercial AC cathode to fabricate a LIC (as shown in Fig. 5a). The electrochemical performance of the AC cathode is depicted in Fig. S8. The AC discharges a specific capacity of 65.1 mA h g^{-1} after 300 cycles at a current density of 0.5 A g^{-1} under a potential range of 2.0–4.3 V with a CE close to 100% (Fig. S8a). Fig. S8b exhibits the rate capacitance of AC, and the capacity still maintains 24.9 mA h g^{-1} even if the current density reaches 5 A g^{-1}. Fig. S8c, d indicate the GCD curves at different current densities and CV curves at different scan rates, respectively. The CV graph is nearly rectangular, thus reflecting the electrostatic adsorption mechanism of the cathode. As the CE of 10-KTi-400@CNFs is low in the first cycle, the 10-KTi-400@CNFs anode was pre-lithiated in the half-cell before assembling LICs. To maintain the charge balance, the mass ratio of the cathode to the anode was set at approximately 4, and the test voltage window was chosen to be 1.0–3.8 V to avoid the oxidative decomposition of the electrolyte. The CV curves of the 10-KTi-400@CNFs//AC LIC at different scan rates are provided in Fig. 5b. The CV curves show a rectangular-like shape with no obvious redox peaks, indicating the ideal capacitive behavior. In

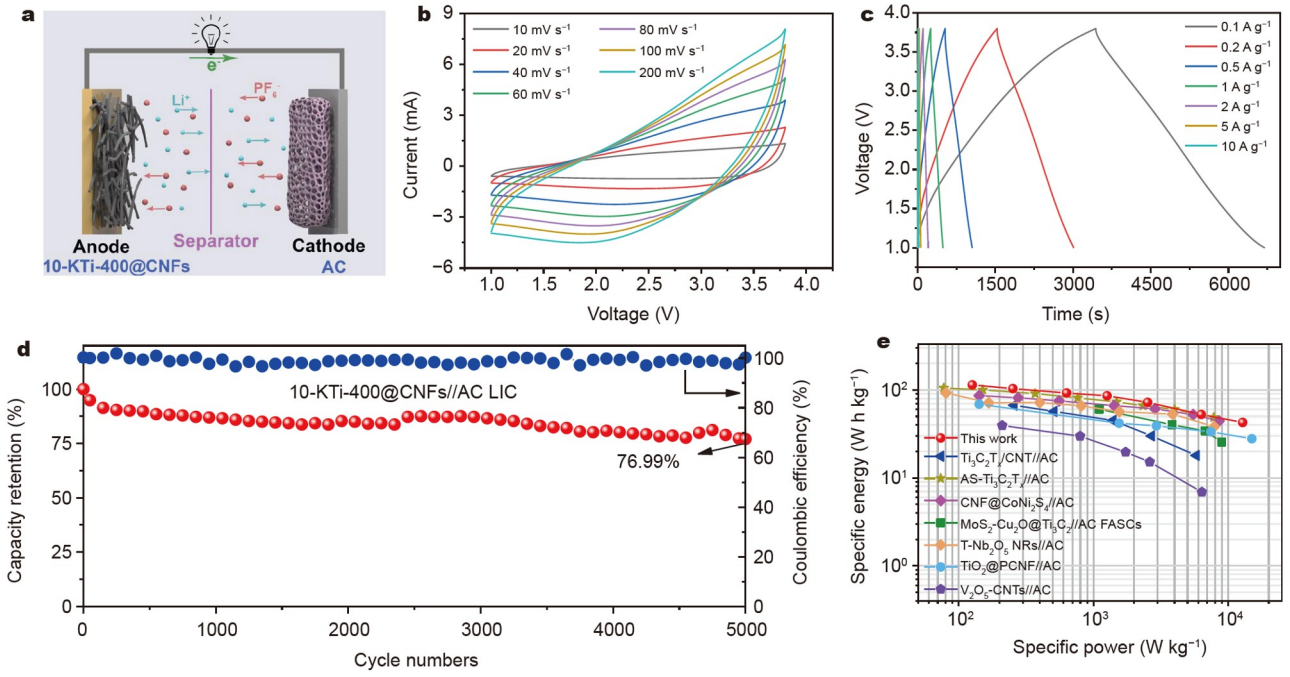

Figure 5 (a) Discharging process of 10-KTi-400@CNFs//AC LIC; (b) CV curves of 10-KTi-400@CNFs//AC LIC at different scan rates; (c) typical GCD profiles of 10-KTi-400@CNFs//AC LIC at different current densities; (d) long-term cycle stability of 10-KTi-400@CNFs//AC LIC at 5 A g^{-1}; (e) Ragone plot for the 10-KTi-400@CNFs//AC LIC based on the total mass of electrodes in comparison with other LICs.

addition, the shape of the CV curve can still be maintained when the scan rate increases, showing high reversibility and good rate performance. Fig. 5c illustrates the GCD curves at different current densities, which are close to the symmetry and correspond to the CV curves. In addition, the capacity retention can still reach 76.99% after 5000 cycles at a current density of 5 A g^{-1} (Fig. 5d). Meanwhile, the CE is almost close to 100% during cycling. Impressively, 10-KTi-400@CNFs//AC LIC exhibited a maximum energy density of 114.3 W h kg^{-1} at a power density of 126.3 W kg^{-1}. Even at a high power density of 12.8 kW kg^{-1}, the energy density can still be maintained at 42.7 W h kg^{-1}. Compared with other capacitors, including $Ti_3C_2T_x$/CNT//AC [48], AS-$Ti_3C_2T_x$//AC [50], CNF@$CoNi_2S_4$//AC [51], MoS_2-Cu_2O@Ti_3C_2//AC [31], T-Nb_2O_5 NRs//AC [52], TiO_2@PCNF//AC [53], and V_2O_5-CNT//AC [54], 10-KTi-400@CNFs//AC LICs offer significant advantages in terms of energy density and power density (Fig. 5e).

The electrochemical reactivity of 10-KTi-400@CNFs//AC LICs was evaluated through XRD and XPS measurements. The XRD patterns of the anode in the initial, fully charged, and discharged states are exhibited in Fig. 6a. When the LIC charged from the initial state to 3.8 V, the (002) peak of Ti_3C_2 shifted to a small angle, indicating that the layer spacing of the 10-KTi-400@CNFs anode increases, which is caused by the embedding of Li^+ ions. When it discharged to 1.0 V, the layer spacing decreased because of the release of Li^+ ions, which is reflected in the right shift of the (002) peak in the XRD. However, it is not possible to completely return to the initial state. During the discharge process, Li^+ ions embedded in the anode materials cannot be completely released due to some irreversible reactions. This condition makes the residual Li^+ exist between the layers of MXene, and the layer spacing slightly increases compared with the initial state.

From the XPS spectra of 10-KTi-400@CNFs (Fig. 6b), the peak intensity of F 1s and P 2p would be weakened, and Li 1s would be enhanced on the XPS patterns during the charging process. As a result, the Li^+ ions were embedded in the anode, whereas PF_6^- was adsorbed onto the cathode under the action of the electrostatic force. The discharge process is the opposite. The histogram of the area shares of the peak intensity represents the content of the Li, F, and P elements. Fig. 6c reflects that the content of Li is 20.1% when the battery is in the initial state, 28.77% when fully charged, and 25.95% when fully discharged, which is consistent with the regularity of the Li^+ ion insertion/extraction in the anode. At the same time, the contents of F and P decreased during the charging process and increased during the discharging process. Fig. 6d, e show the XPS spectra and element contents of the cathode, respectively. When charging to 3.8 V, the content of F and P increased to 19.59% and 1.96% (0.17% and 0.07% in the initial state, respectively) due to the adsorption of PF_6^- from the electrolyte to the cathode. When discharging to 1.0 V, the peak intensities of F 1s and P 2p decreased, where the elemental contents were 2.93% and 0.67%, respectively, confirming that PF_6^- is desorbed from the cathode back into the electrolyte. Importantly, according to the charge balance principle, more Li^+ ions exist near the cathode during the discharging process compared with the charging process. Meanwhile, the content of Li increased from 20.69% to 23.49%. In a word, the mechanism of LICs is demonstrated as the Li^+ ions are embedded in the anode, while PF_6^- is adsorbed onto the cathode under the action of the electrostatic force during the charging process. In addition, due to the formation of the Ti–O–C bond in the anode, the rapid transmission of electrons is ensured, the 3D transmission channels of ions are set up, and the capacitive performance of the 10-KTi-400@CNFs composites is improved, which enhances the 10-KTi-400@CNFs//AC LICs'

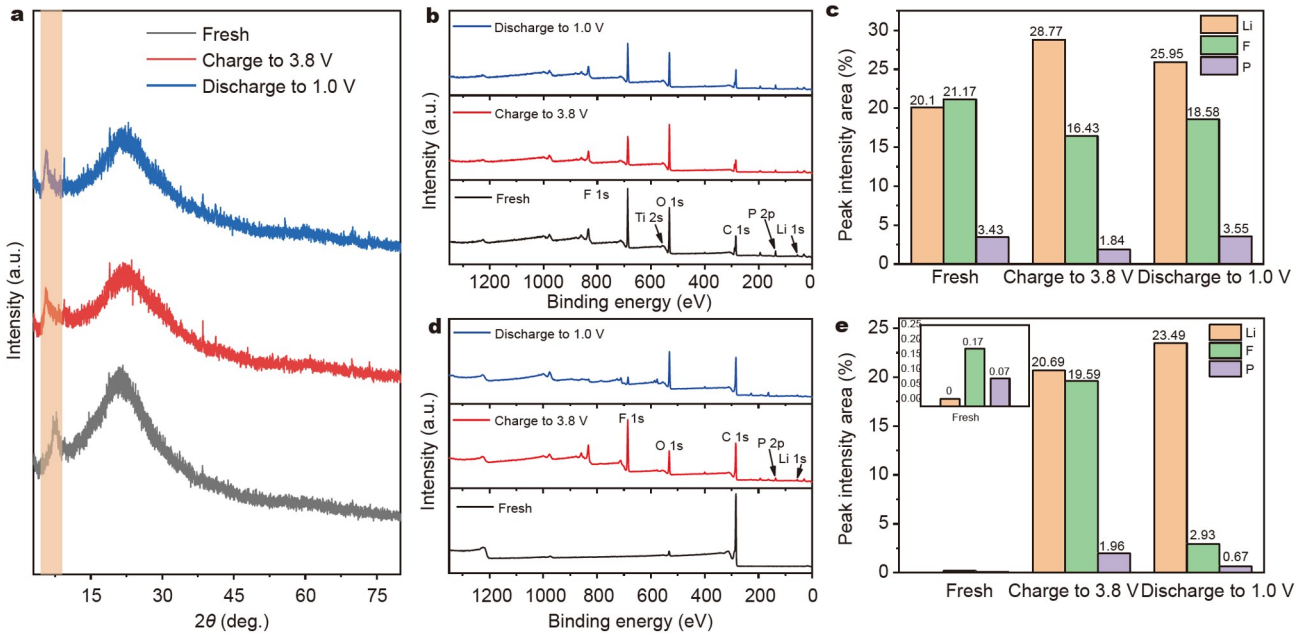

Figure 6 Charge/discharge mechanism of 10-KTi-400@CNFs//AC LICs at fresh, fully discharged, and fully charged states. (a) XRD patterns and (b) XPS spectra of the 10-KTi-400@CNFs anode; (c) peak intensity area shares of Li, P, and F in the XPS spectrum of the 10-KTi-400@CNFs anode; (d) XPS spectra of the AC cathode; (e) peak intensity area shares of Li, P, and F in the XPS spectrum of the AC cathode.

electrochemical performance.

CONCLUSIONS

In summary, flexible 10-KTi-400@CNFs film electrodes were prepared *via* a simple electrospinning strategy. The remarkable merits of smooth 3D electron/ion transport channels, enhanced ion storage capability, and large, accessible specific surface area are credited to the Ti–O–C chemical bond formation, oxygen-containing functional group modification, and K^+ ion intercalation, respectively. They also endow the 10-KTi-400@CNFs film electrodes with enhanced lithium-ion storage capability in hybrid capacitors. By being coupled with the AC cathode, the 10-KTi-400@CNFs//AC LICs exhibit a remarkable energy density of 126.3 W kg^{-1} at 114.3 W h kg^{-1}, an exceptional power density of 12.8 kW kg^{-1} at 42.7 W h kg^{-1}, and a high capacity retention of 76.99% after 5000 cycles. The strategy proposed in this study can also be applied in other MXene-based materials, providing a new idea to design suitable pseudocapacitance characteristics to improve the energy storage performance of LICs.

Received 2 August 2022; accepted 21 September 2022; published online 7 December 2022

1 Larcher D, Tarascon JM. Towards greener and more sustainable batteries for electrical energy storage. Nat Chem, 2015, 7: 19–29
2 Xu H, Zheng R, Du D, *et al.* Cationic vanadium vacancy-enriched $V_{2-x}O_5$ on V_2C mxene as superior bifunctional electrocatalysts for Li-O_2 batteries. Sci China Mater, 2022, 65: 1761–1770
3 Ding J, Hu W, Paek E, *et al.* Review of hybrid ion capacitors: From aqueous to lithium to sodium. Chem Rev, 2018, 118: 6457–6498
4 Du Y, Wang X, Zhang Y, *et al.* High mass loading CaV_4O_9 microflowers with amorphous phase transformation as cathode for aqueous zinc-ion battery. Chem Eng J, 2022, 434: 134642
5 Wang H, Zhu C, Chao D, *et al.* Nonaqueous hybrid lithium-ion and sodium-ion capacitors. Adv Mater, 2017, 29: 1702093
6 Jin L, Shen C, Shellikeri A, *et al.* Progress and perspectives on pre-lithiation technologies for lithium ion capacitors. Energy Environ Sci, 2020, 13: 2341–2362
7 Chen P, Zhou W, Xiao Z, *et al. In situ* anchoring MnO nanoparticles on self-supported 3D interconnected graphene scroll framework: A fast kinetics boosted ultrahigh-rate anode for Li-ion capacitor. Energy Storage Mater, 2020, 33: 298–308
8 Dong S, Li H, Wang J, *et al.* Improved flexible Li-ion hybrid capacitors: Techniques for superior stability. Nano Res, 2017, 10: 4448–4456
9 Er D, Li J, Naguib M, *et al.* Ti_3C_2 MXene as a high capacity electrode material for metal (Li, Na, K, Ca) ion batteries. ACS Appl Mater Interfaces, 2014, 6: 11173–11179
10 Gao X, Du X, Mathis TS, *et al.* Maximizing ion accessibility in MXene-knotted carbon nanotube composite electrodes for high-rate electrochemical energy storage. Nat Commun, 2020, 11: 6160
11 Chao H, Li Y, Lu Y, *et al.* MXene-mediated regulation of local electric field surrounding polyoxometalate nanoparticles for improved lithium storage. Sci China Mater, 2022, 65: 2958–2966
12 Hu M, Zhang H, Hu T, *et al.* Emerging 2D MXenes for supercapacitors: Status, challenges and prospects. Chem Soc Rev, 2020, 49: 6666–6693
13 Zhang M, Cao J, Wang Y, *et al.* Electrolyte-mediated dense integration of graphene-MXene films for high volumetric capacitance flexible supercapacitors. Nano Res, 2020, 14: 699–706
14 Shao Y, El-Kady MF, Sun J, *et al.* Design and mechanisms of asymmetric supercapacitors. Chem Rev, 2018, 118: 9233–9280
15 Tian Y, Que B, Luo Y, *et al.* Amino-rich surface-modified MXene as anode for hybrid aqueous proton supercapacitors with superior volumetric capacity. J Power Sources, 2021, 495: 229790
16 Xiao Z, Zhao L, Yu Z, *et al.* Multilayered graphene endowing superior dispersibility for excellent low temperature performance in lithium-ion capacitor as both anode and cathode. Chem Eng J, 2022, 429: 132358
17 Li FF, Gao JF, He ZH, *et al.* Design and synthesis of CoP/r-GO hierarchical architecture: Dominated pseudocapacitance, fasted kinetics features, and Li-ion capacitor applications. ACS Appl Energy Mater, 2020, 3: 5448–5461
18 Wang L, Zhang X, Xu Y, *et al.* Tetrabutylammonium-intercalated 1T-MoS_2 nanosheets with expanded interlayer spacing vertically coupled on 2D delaminated MXene for high-performance lithium-ion capacitors. Adv Funct Mater, 2021, 31: 2104286

19 Li T, Zhang J, Li C, *et al.* Nitrogen and phosphorous co-doped hierarchical meso—Microporous carbon nanospheres with extraordinary lithium storage for high-performance lithium-ion capacitors. Sci China Mater, 2022, 65: 2363–2372
20 Luo B, Hu Y, Zhu X, *et al.* Controllable growth of SnS_2 nanostructures on nanocarbon surfaces for lithium-ion and sodium-ion storage with high rate capability. J Mater Chem A, 2018, 6: 1462–1472
21 Li X, Huang Z, Shuck CE, *et al.* MXene chemistry, electrochemistry and energy storage applications. Nat Rev Chem, 2022, 6: 389–404
22 Chen J, Ding Y, Yan D, *et al.* Synthesis of MXene and its application for zinc-ion storage. SusMat, 2022, 2: 293–318
23 VahidMohammadi A, Rosen J, Gogotsi Y. The world of two-dimensional carbides and nitrides (MXenes). Science, 2021, 372: 1165
24 Ghidiu M, Lukatskaya MR, Zhao MQ, *et al.* Conductive two-dimensional titanium carbide 'clay' with high volumetric capacitance. Nature, 2014, 516: 78–81
25 Naguib M, Halim J, Lu J, *et al.* New two-dimensional niobium and vanadium carbides as promising materials for Li-ion batteries. J Am Chem Soc, 2013, 135: 15966–15969
26 Zhang T, Zhang L, Hou Y. MXenes: Synthesis strategies and lithium-sulfur battery applications. eScience, 2022, 2: 164–182
27 Zhang K, Zhao D, Qian Z, *et al.* N-doped $Ti_3C_2T_x$ MXene sheet-coated SiO_x to boost lithium storage for lithium-ion batteries. Sci China Mater, 2023, 66: 51–60
28 Bao W, Tang X, Guo X, *et al.* Porous cryo-dried MXene for efficient capacitive deionization. Joule, 2018, 2: 778–787
29 Guo Y, Zhang D, Yang Y, *et al.* MXene-encapsulated hollow Fe_3O_4 nanochains embedded in N-doped carbon nanofibers with dual electronic pathways as flexible anodes for high-performance Li-ion batteries. Nanoscale, 2021, 13: 4624–4633
30 Song X, Wang H, Jin S, *et al.* Oligolayered $Ti_3C_2T_x$ MXene towards high performance lithium/sodium storage. Nano Res, 2020, 13: 1659–1667
31 Mao X, Zou Y, Xu F, *et al.* Three-dimensional self-supporting Ti_3C_2 with MoS_2 and Cu_2O nanocrystals for high-performance flexible supercapacitors. ACS Appl Mater Interfaces, 2021, 13: 22664–22675
32 Yi S, Wang L, Zhang X, *et al.* Cationic intermediates assisted self-assembly two-dimensional Ti_3C_2T/rGO hybrid nanoflakes for advanced lithium-ion capacitors. Sci Bull, 2021, 66: 914–924
33 He X, Jin S, Miao L, *et al.* A 3D hydroxylated MXene/carbon nanotubes composite as a scaffold for dendrite-free sodium-metal electrodes. Angew Chem Int Ed, 2020, 59: 16705–16711
34 Luo J, Zhang W, Yuan H, *et al.* Pillared structure design of MXene with ultralarge interlayer spacing for high-performance lithium-ion capacitors. ACS Nano, 2017, 11: 2459–2469
35 Huang P, Zhang S, Ying H, *et al.* Fabrication of Fe nanocomplex pillared few-layered $Ti_3C_2T_x$ MXene with enhanced rate performance for lithium-ion batteries. Nano Res, 2020, 14: 1218–1227
36 Li J, Yuan X, Lin C, *et al.* Achieving high pseudocapacitance of 2D titanium carbide (MXene) by cation intercalation and surface modification. Adv Energy Mater, 2017, 7: 1602725
37 Levitt AS, Alhabeb M, Hatter CB, *et al.* Electrospun MXene/carbon nanofibers as supercapacitor electrodes. J Mater Chem A, 2019, 7: 269–277
38 Chen X, Zhu Y, Zhang M, *et al.* *n*-Butyllithium-treated $Ti_3C_2T_x$ MXene with excellent pseudocapacitor performance. ACS Nano, 2019, 13: 9449–9456
39 Zhang CJ. Interfacial assembly of two-dimensional mxenes. J Energy Chem, 2021, 60: 417–434
40 Shi H, Zhang P, Liu Z, *et al.* Ambient-stable two-dimensional titanium carbide (MXene) enabled by iodine etching. Angew Chem Int Ed, 2021, 60: 8689–8693
41 Naguib M, Kurtoglu M, Presser V, *et al.* Two-dimensional nanocrystals produced by exfoliation of Ti_3AlC_2. Adv Mater, 2011, 23: 4248–4253
42 Tang J, Peng X, Lin T, *et al.* Confining ultrafine tin monophosphide in $Ti_3C_2T_x$ interlayers for rapid and stable sodium ion storage. eScience, 2021, 1: 203–211
43 An GH, Koo BR, Ahn HJ. Activated mesoporous carbon nanofibers fabricated using water etching-assisted templating for high-performance electrochemical capacitors. Phys Chem Chem Phys, 2016, 18: 6587–6594
44 Yang C, Ren J, Zheng M, *et al.* High-level N/P co-doped Sn-carbon nanofibers with ultrahigh pseudocapacitance for high-energy lithium-ion and sodium-ion capacitors. Electrochim Acta, 2020, 359: 136898
45 Zhou J, Xu S, Kang Q, *et al.* Iron oxide encapsulated in nitrogen-rich carbon enabling high-performance lithium-ion capacitor. Sci China Mater, 2020, 63: 2289–2302
46 Yang L, Qin H, Dong Z, *et al.* Metallic S-CoTe with surface reconstruction activated by electrochemical oxidation for oxygen evolution catalysis. Small, 2021, 17: 2102027
47 Jin H, Li J, Xu Z, *et al.* Assembly of two-dimensional nanofluidic channel with high proton conductivity using single-layer MnO_2 nanosheets. Sci China Mater, 2022, 65: 2578–2584
48 Yu P, Cao G, Yi S, *et al.* Binder-free 2D titanium carbide (MXene)/carbon nanotube composites for high-performance lithium-ion capacitors. Nanoscale, 2018, 10: 5906–5913
49 Qiu ZM, Bai Y, Gao YD, *et al.* MXenes nanocomposites for energy storage and conversion. Rare Met, 2021, 41: 1101–1128
50 Xia Y, Que LF, Yu FD, *et al.* Boosting ion/e^- transfer of Ti_3C_2 *via* interlayered and interfacial co-modification for high-performance Li-ion capacitors. Chem Eng J, 2021, 404: 127116
51 Jagadale A, Zhou X, Blaisdell D, *et al.* Carbon nanofibers (CNFs) supported cobalt- nickel sulfide ($CoNi_2S_4$) nanoparticles hybrid anode for high performance lithium ion capacitor. Sci Rep, 2018, 8: 1602
52 Qin L, Liu Y, Xu S, *et al.* In-plane assembled single-crystalline T-Nb_2O_5 nanorods derived from few-layered Nb_2CT_x MXene nanosheets for advanced Li-ion capacitors. Small Methods, 2020, 4: 2000630
53 Ju J, Lv Y, An X, *et al.* The stereoscopic honeycomb-like porous carbon nanofibers as a carrier of TiO_2 nanoparticles for high-performance Li-ion capacitor. J Alloys Compd, 2019, 791: 1248–1256
54 Sathiya M, Prakash AS, Ramesha K, *et al.* V_2O_5-anchored carbon nanotubes for enhanced electrochemical energy storage. J Am Chem Soc, 2011, 133: 16291–16299

Acknowledgements This work was supported by the National Natural Science Foundation of China (22005167 and 21905152), Shandong Provincial Natural Science Foundation (ZR2020QB125 and ZR2020MB045), China Postdoctoral Science Foundation (2021M693256, 2021T140687 and 2022M713249), Qingdao Postdoctoral Applied Research Project, Taishan Scholar Project of Shandong Province (ts20190937), and the Youth Innovation Team Project for Talent Introduction and Cultivation in Universities of Shandong Province.

Author contributions Wang X planned and designed the project; Feng M performed all the experiments and analyzed the data; Wang X and Feng M wrote this paper; Liu Z provided some guidance and suggestions on the experiments; Wang W and Hu Z helped to synthesize the materials; Fan C and Zhao X helped to characterize the samples; Wang P provided suggestions on the experiments; Li H and Yang L provided guidance on the paper. All the authors contributed to the general discussion.

Conflict of interest The authors declare that they have no conflict of interest.

Supplementary information Supporting data are available in the online version of the paper.

Min Feng is currently a Master's student at Qingdao University of Science and Technology, under the guidence of associate professor Xiaojun Wang. Her research focuses on the preparation of $Ti_3C_2T_x$ (MXene)-based composite nanomaterials and their applications in energy storage fields.

Xiaojun Wang is currently an associate professor at the College of Electromechanical Engineering, Qingdao University of Science and Technology. She received her PhD degree from Nankai University in 2019 and then continued with her post-doctoral research at Qingdao Institute of Bioenergy and Bioprocess Technology, Chinese Academy of Sciences. Her research interests include advanced energy storage materials and devices, such as sodium-ion batteries and zinc-ion batteries.

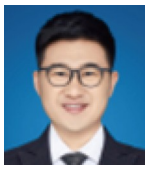

Zhiming Liu is currently a professor at Qingdao University of Science and Technology. He earned his PhD degree in energy engineering from Hanyang University in Korea in 2018 and then continued his post-doctoral research under the supervision of Dr. Guanglei Cui at Qingdao Institute of Bioenergy and Bioprocess Technology, Chinese Academy of Sciences. His research focuses on functional nanomaterials for electrochemical energy storage and conversion.

具有三维传输通道的化学键合Ti_3C_2 MXene@C复合材料促进混合电容器中的锂离子存储

冯敏[1], 王万里[1], 胡兆伟[1], 范呈[1], 赵晓冉[1], 王朋[1], 李慧芳[1], 杨磊[2,3], 王晓君[1,3*], 刘治明[1*]

摘要 锂离子电容器(LICs)是一种很有前途的储能装置, 因为它们同时具有锂离子电池的高能量密度和超级电容器的高功率密度的特点. 然而, 由于锂离子电容器中阳极和阴极之间电化学反应动力学的不匹配, 使得探索具有快速离子扩散和电子转移通道的阳极材料面临挑战. 在此, 通过静电纺丝策略将具有可控末端基团的二维Ti_3C_2 MXene引入一维碳纳米纤维中, 形成三维导电网络. 在这种Ti_3C_2 MXene和碳基复合材料(称为KTi-400@CNFs)中, 二维纳米片结构赋予了Ti_3C_2 MXene更多Li^+存储活性位点, 而碳骨架则有利于提高复合材料的导电性. 更值得一提的是, 在Ti_3C_2 MXene和碳骨架的界面上形成了Ti–O–C键. 复合材料中的这种化学键为电子的快速传输和离子在层与层之间纵向的快速扩散建立了桥梁. 因此, 优化后的KTi-400@CNFs复合材料在电流密度为5 A g^{-1}的情况下, 500次循环后仍保持235 mA h g^{-1}的良好容量. 由KTi-400@CNFs//AC组成的锂离子电容器实现了高能量密度(114.3 W h kg^{-1})和高功率密度(12.8 kW kg^{-1}). KTi-400@CNFs的这种独特结构和优异的电化学性能为二维材料制备提供了参考.